Supplementary Information: Nanophotonic waveguide chip-to-free-space beam scanning at 68M Spots/s·mm²

Matt Saha[*,1], Y. Henry Wen,[*,1,α] Andrew S. Greenspon[*,1,2], Matthew Zimmermann[*,1], Kevin J. Palm[1,2], Alex Witte[1], Yin Min Goh[2], Chao Li[2], Mark Dong[1,2], Andrew J. Leenheer[3], Genevieve Clark[1,2], Gerald Gilbert[4,⁑], Matt Eichenfield[3,5,&], and Dirk Englund[2,†]

These authors contributed equally to this work.

[1]*The MITRE Corporation, 202 Burlington Road, Bedford, Massachusetts 01730, USA*
[2]*Research Laboratory of Electronics, Massachusetts Institute of Technology, Cambridge, Massachusetts 02139, USA*
[3]*Sandia National Laboratories, P.O. Box 5800 Albuquerque, New Mexico 87185, USA*
[4]*The MITRE Corporation, 200 Forrestal Road, Princeton, New Jersey 08540, USA*
[5]*College of Optical Sciences, University of Arizona, Tucson, Arizona 85719, USA*
[α]*hwen@mitre.org*, [⁑]*ggilbert@mitre.org*,[&]*eichenfield@arizona.edu*, [†]*englund@mit.edu*

SI-1. Film stresses and the effect of cross-ribs on ski-jump curling behavior

Though the material stress in the SiO_2 layers is moderately compressive, the aluminum nitride (AlN) passive stress profile is a gradient from moderately compressive to moderately tensile (from bottom to top). The stresses of the Al electrodes are negligible, and the silicon nitride (Si_3N_4) stress is highly compressive. As a result, a released cantilever containing just bottom SiO_2 and Al-AlN-Al curls moderately upward due to the combination of underlying compressive and overlaying tensile stresses. The stresses are linear, so longer and wider cantilevers will curl up to a larger final angle. Because the Si_3N_4 deposited is highly compressive, increasing the thickness of the Si_3N_4 or the number of Si_3N_4 waveguides diminishes the cantilever's curvature. Similarly, uniformly increasing the amount of SiO_2 above the top electrode functions to reduce passive curvature. Ordinarily, this would suggest that all cladding above the top electrode should be removed aside from a small cladding buffer around the waveguides; namely, the pad open etch (POE) design.

However, if this top SiO_2 cladding is instead patterned into lateral cross-ribs rather than being removed entirely, the device curvature can be further enhanced. We qualitatively explain this phenomenon here as follows: for POE devices, the material stresses are not optimally directed along the length of the cantilever to produce the desired longitudinal curvature. Rather, these devices exhibit undesired upward lateral curling along their width, also in part due to the concentrated compressive stress of the waveguide(s) located along the cantilever's midline. By designing devices with SiO_2 cross-ribs, lateral upwards curvature is diminished, and the stress is more efficiently directed to enhance longitudinal curvature. The degree to which this cross-rib patterning affects device curvature can also be adjusted by changing the cross-rib period and cross-rib duty cycle. Broadly, we observed enhanced longitudinal curvature by increasing the cross-rib period and decreasing the cross-rib duty cycle. However, though the cross-ribs are useful in redirecting the material stresses, the SiO_2 is still compressive. Thus, an ideal cross-rib pattern strikes a balance between the total amount of top cladding and the periodic restraint of upward lateral curvature. For 0.75 μm wide cross-ribs, the optimal cross-rib period was found to be between 4 μm and 8 μm (Fig. 2f). We also note that cross-rib patterned devices were overall more uniform in their curling behavior across the wafer when compared to the POE design.

SI-2. Stroboscopic Imaging

To better understand the mechanical mode shapes of the cantilever resonances, stroboscopic imaging was used. While driving a ski-jump on one of its resonance frequencies, a fiber-coupled supercontinuum white light laser (NKT Photonics SuperK COMPACT) was pulsed at approximately the same frequency, with a frequency offset < 5Hz, and directed onto the PIC surface with a Thorlabs achromatic fiber collimator (C80APC-A, f = 80 mm, FC/APC, ARC: 400 - 650 nm). These stroboscopic videos were captured using a mirrorless camera (Nikon Z7 II) equipped with a macro lens (Venus Laowa 25mm, f/2.8, 2.5-5x). A few examples are provided as Supplementary Videos 1-3. To stroboscopically image the ski-jump tracing a 2D Lissajou pattern (Supplementary Video 5), the X and Y driving frequencies were set to a rational ratio (4.86 kHz:6.48 kHz → 3:4), and the white light was pulsed at approximately the same frequency as the refresh rate of the pattern (~1.62 kHz). Note that, in these videos, a set of 3 devices are being actuated with the same drive signals. These cantilevers have different widths which cause their resonance frequencies to differ. As a result, only one cantilever (furthest from the camera) is being driven directly on-resonance.

SI-3. 1D ambient, vacuum, and cryogenic device characterization

Fig. S1 shows the experimental setup for characterizing the 1D beam steering behavior of the ski-jump (as shown in Fig. 3) at ambient pressure, various vacuum pressures, and cryogenic temperatures. The sample is mounted on a holder with an attached printed circuit board (PCB) and has wire bonds to ground-signal-ground (GSG) pads with an SMA feedthrough. This holder is mounted on a fixed stage in a Montana CryoAdvance 100 cryostat with a nominal base temperature of 4 K. A fiber feedthrough into the cryostat allows for placement of a lensed fiber on a 3-axis stage. This enables precise edge coupling to an on-chip waveguide that routes light into the ski-jump. A 730 nm laser diode was used for intensified charged coupled device (ICCD) measurements, and a 532 nm Cobolt continuous wave diode pumped laser was used for position sensitive detector (PSD) measurements as it provided a sufficiently powerful optical signal.

In order to analyze control capabilities and beam quality, the optical output of the waveguide embedded on ski-jump was collected through the cryostat glass window into a 50X long working distance (LWD) objective (50X Mitutoyo Plan Apo NIR Infinity Corrected Objective, NA = 0.42, WD = 17 mm). The light could then be routed a 1) CMOS camera [Thorlabs CS165CU Zelux® 1.6 MP Color CMOS Camera], 2) high-speed ICCD [Andor DH334T-18U-63], or 3) PSD [Thorlabs PDQ80A - Quadrant Detector, 400 to 1050 nm, detector bandwidth 150 kHz]. The CMOS camera is primarily used to view the devices in the cryostat, align the edge-coupled fiber, and align the output of the ski-jump into the free-space optical path. A 4f optical relay composed of two 300 mm lenses was used due to the long optical path in the setup. A 150 mm lens was used to image the ski-jump output onto the ICCD. During measurements with the ICCD, the device was driven using an arbitrary waveform generator (Siglent SDG6052X), optionally connected to a voltage amplifier (PiezoDrive PD200x4 Voltage Amplifier) depending on the desired voltages.

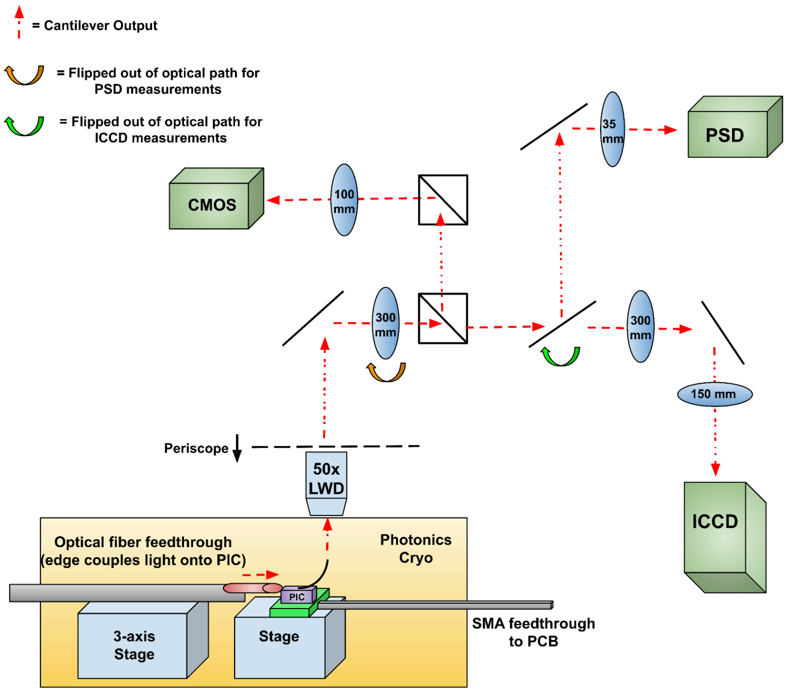

Fig. S1 | Experimental setup used to characterize one-dimensional beam steering of the ski-jump device at ambient, vacuum, and cryogenic conditions.

A single focusing lens (f = 35 mm) was used to image the beam onto the PSD with no 4f relay included in the path. To collect frequency response data, we used the PSD connected to a Moku:Pro Multifunction Signal Generator and Analyzer. This tool could 1) measure the frequency response by sweeping drive frequency and measuring received power at that frequency (or its harmonics), 2) transmit a specific drive frequency and measure the device's broadband frequency response as a result, or 3) function as an oscilloscope for ring-down measurements. The frequency response toolbox originally compared received power to transmitted power as $S21_{db}(f)=10*log10(P_{RX}(f)/P_{TX}(f))$; this was converted to a voltage enhancement factor $V_{enh}(f)=10^{S21\_db/20}$, normalized by dividing by the low frequency response at 100 Hz, and converted to decibels as $V_{enh\_norm\_dB}(f)=10*log10(V_{enh\_norm}(f))$.

For ambient pressure and rough vacuum, we measure the quality (Q) factor by taking the full width at half maximum (FWHM) of a Lorentzian fitted peak over each resonance's $V_{enh,norm}(f)$. At high vacuum, we see a large increase in the resonance enhancements and observe resonances up to the 150 kHz bandwidth limit of the photodetector. Here, we calculate the Q factors by monitoring the ring-down of a signal after turning off the AC input and then calculating the exponential decay time constant τ and mechanical Q factor as $Q = \pi f_0 \tau$, where f_0 is the resonance frequency.

The frequency response plots are stitched together from frequency response datasets taken at various drive voltages. To measure large enhancement at certain frequencies, the drive voltage was decreased to avoid saturation. To measure a clean response close to the noise floor, the drive voltage was increased proportionally. For both high and low voltage sweeps, data was normalized with respect to the low frequency response and stitched together to show both the noise floor and high enhancement. Table S1 details resonant frequencies, enhancements, and measured quality factors.

Table S1 Mechanical resonance characterization

	Atmospheric Pressure			Rough Vacuum (1.15 Torr)			High Vacuum (<0.1 mTorr)			Cryogenic (6.9K, <0.1 mTorr)		
Resonances	**Freq (kHz)**	**Enh (dB)**	**Q**	**Freq (kHz)**	**Enh (dB)**	**Q**	**Freq (kHz)**	**Enh (dB)**	**Q**	**Freq (kHz)**	**Enh (dB)**	**Q**
1st Y	1.16	10	5.4	1.23	15.3	24.4	1.22	30	~10000[a]	1.28	18.1	2000[a]
2nd Y	5.75	2.9	12.2	6.17	13	101.3	6.01	23.4	~6800[a]	3.98	17.2	3000[a]
3rd Y	17.98	0	14.9	18.9	10.6	246.6	18.66	16.7				
4th Y	36.31	-9.6	13.6	37.4	4.2	415.4	36.96	11.6				
1st X	3.74	-4.8	19.8	3.97	3.7	110.4	3.87	15.6	~11000[a]	2.72	12.9	8300[a]
2nd X	28.4	-13.7	45.3	30	-4	635.2	29.33	-0.4				

Q factor is measured from signal ring-down rather than FWHM. [a]

To verify the device performance stability with cryogenic cycling, we measure the frequency response with the PSD both before and after cooling it to a cryogenic temperature of ~ 6.9 K. When compared to room temperature, we observed red-shifting of the resonant frequencies. Although the device's curling and resonant frequencies had shifted when at 6.9 K, we verified that the device curvature, resonant frequencies, and enhancement factors returned to their original values after the device returned to room temperature.

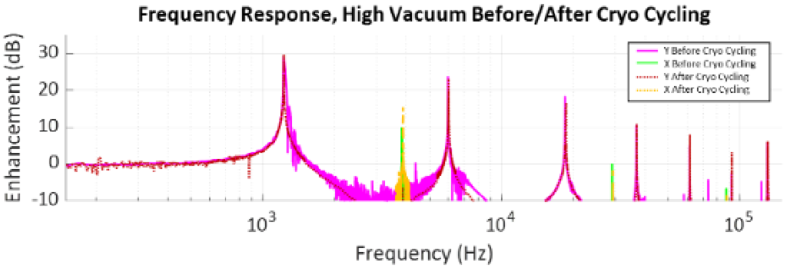

Fig. S2 | Ski-jump frequency response data at high vacuum before and after cryo cycling the device down to 6.9 K.

In order to demonstrate broadband frequency use of the ski-jump, we placed the photonic integrated circuit (PIC) on a room temperature setup similar to that shown in Fig. S1 but without a cryostat. A supercontinuum white light laser (NKT Photonics SuperK COMPACT) was connected to a tunable wavelength filter (SuperK Varia), providing 400 nm - 800 nm visible pulsed laser light. This optical signal was edge coupled to the PIC waveguide which routes to the ski-jump device. For the images shown in Fig. 3g, the ski-jump was driven at its second longitudinal resonance of 6.75 kHz with a 40 Vpp sinusoidal signal. Beam streaks were collected on a Thorlabs color CMOS camera at several different wavelengths to show identical scanning ranges of ~40 µm under these conditions.

To observe time-resolved motion of the resonantly scanning beam, the ICCD was gated with pulses much shorter than the device's period of motion and synced with the drive signal of the cantilever. The time offset between these gate pulses and the device's drive signal was stepped up between each frame. For each acquisition/frame, many gate pulses were integrated over, with each gate occurring periodically at the device's driving frequency, to achieve sufficient counts for a clear image. An example time-resolved video of a device's 2nd order Y resonance (ambient conditions) is included as Supplementary Video 4. In this example, the ICCD was gated with 200 ns pulses with a 0.7 µs time step between frames.

To characterize DC actuation, DC voltages were applied to the ski-jump, and surface profile measurements of the device were obtained using an optical profilometer (Bruker ContourX-100).

SI-4. 2D ambient beam steering characterization and image projection

Single electrode devices have AlN sandwiched between uniform layers of Al. The split-electrode devices share a common ground plane of bottom Al metal. The top Al metal was split in half across the longitudinal midline of the cantilever, with connections to separate GSG pads sharing a common ground. This allowed for independent amplitude and phase control for each half of the device.

A setup similar to that shown in Fig. S1 was used to characterize the split-electrode device and to demonstrate 2D image and video projection. The wire-bonded sample and fiber array are each mounted on 3-axis stages to optimize edge coupling. A lensed fiber is used to couple laser light into the PIC waveguide that routes to the ski-jump device. For data collection with the PSD and ICCD, a Hübner Photonics C-Wave GTR tunable laser set to 737 nm was used. For arbitrary image projection, a 532 nm Cobolt laser was connected to a fiber-coupled AOM to modulate the ski-jump's optical signal. To generate the necessary pulse sequence, a custom MATLAB script takes an image as an input and generates the necessary AOM pulse sequence for a given set of X and Y drive voltages and phases.

SI-5. Electrical Analysis:

The DC resistance of the device was measured with a Keithley 6487 Picoammeter, which measures the current after applying a set voltage and converts to a resistance. We measure a resistance of >40 GΩ with a ±20 V signal applied but also observe the resistance drop as the voltage amplitude and applied cantilever strain increase. At ±50 V, we measure ~1 GΩ.

The AC electrical response was measured with a Keysight E5061B Impedance Analyzer. We collect the S11 response, convert to a complex impedance, and fit the imaginary portion of the complex impedance to the equation $Im(Z) = \frac{-1}{2\pi f C}$ where f is the driving frequency and C is the capacitance. This gives a measured capacitance of 36.6 pF for a set of 3 ski-jump devices, a good match with the calculated capacitance of 30.5 pF based on the equation for a parallel plate capacitor: $C = \frac{e_0 e_r A}{d}$, where e_0 = 8.85e-12 F/m, e_r = 9 (dielectric constant for AlN), d = 450e-9 m, and A = 172e-7 m^2. Since this capacitance includes three devices in one test socket, the average capacitance of a single ski-jump is ~10.2 pF.

SI-6. Second Harmonic Resonances

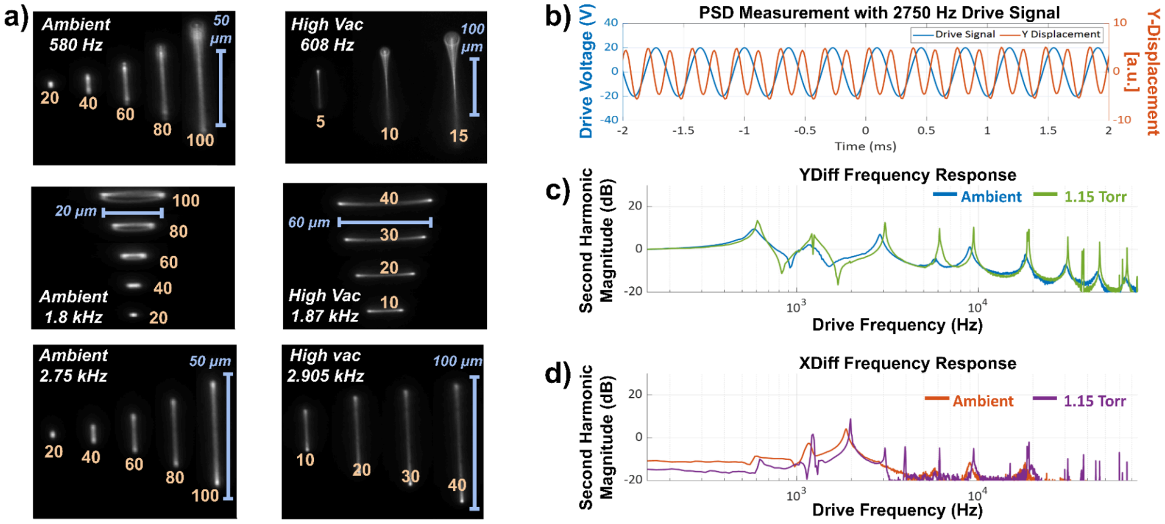

Fig. S3 | Second harmonic resonance data. **a)** ICCD data showing large displacement at half the resonant frequencies of certain modes. **b)** Position-sensitive detector measurement of the projected beam displacement while driving with a 2750 Hz signal, showing the displacement oscillating at 5500 Hz. **c, d)** Frequency Response Measurement from Position Sensitive Detector of the second harmonic magnitude at ambient and vacuum

Measuring the beam tip with the ICCD or the PSD, we observe several "second harmonic resonances". In these cases, driving the cantilever at certain frequencies produces a response that shows high displacement at twice the drive frequency. These often also correspond to dips in the (fundamental) frequency response measurements. For example, driving a ski-jump at 2.75 kHz while monitoring the beam tip position produces little response at 2.75 kHz. Rather, a strong response at 5.5 kHz is observed. This "second harmonic resonance" motion also lines up with the known longitudinal mode at ~ 5.5 kHz that can be excited directly using a 5.5 kHz drive signal. This can also be seen in time-resolved imaging of the beam at this resonance in ambient conditions (Supplementary Video 7).

Comparing the second harmonic response of the longitudinal displacement shown in Fig. S3c, we see a small second harmonic component of our known resonances at 1.2 kHz, 5.5 kHz, and 18 kHz. However, we also observe a strong second harmonic component at half those frequencies (around 0.6 kHz, 2.75 kHz, and 9 kHz, respectively). These frequencies did not produce a strong response at the original drive frequencies, so we note these as "second harmonic resonances". Lateral displacement modes can show similar behavior, as seen in the ~3.6 kHz oscillation using a 1.8 kHz drive signal.

These second harmonic resonances could be a result of the strain response in the cantilever bimorph, which will have significant higher-order harmonics in the frequency domain. If these are amplified by the mechanical response of the cantilever, particularly on resonances with high enhancement, it could explain the cantilever's oscillation at twice the drive frequency.

SI-7. Experimental setup for ski-jump projection to diamond chiplet emitters

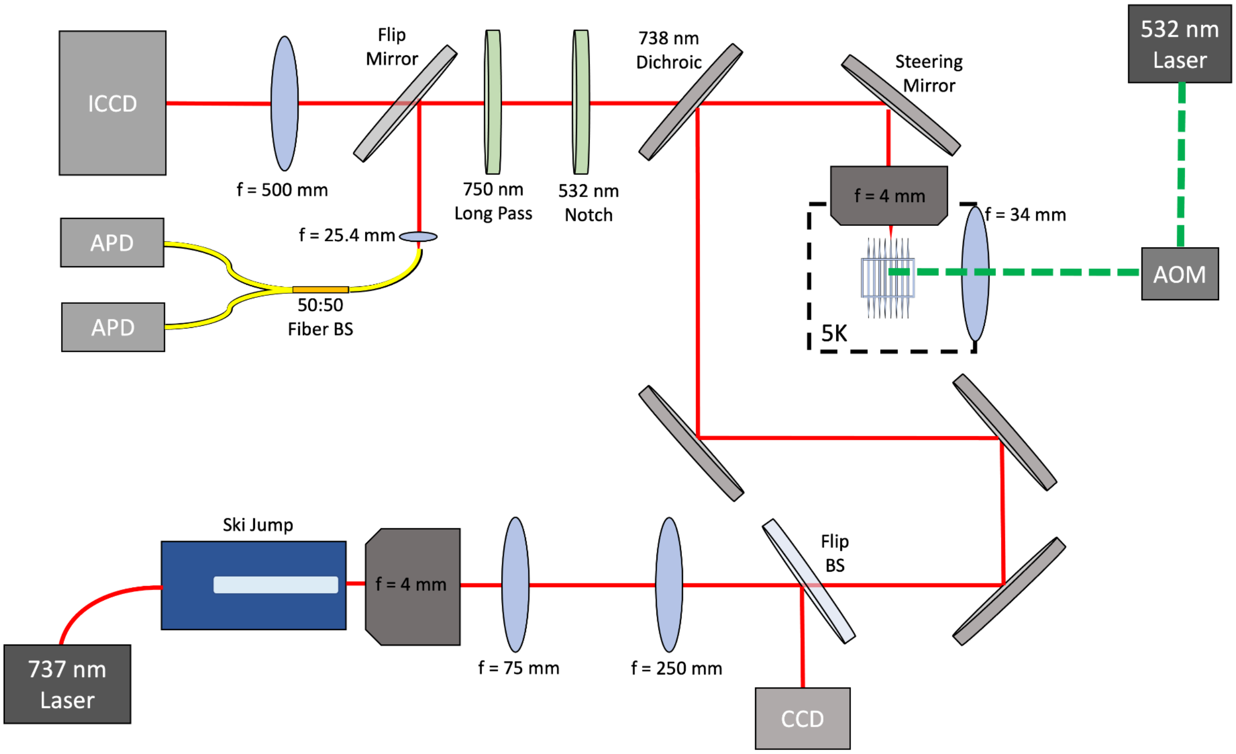

Fig. S4 | Experimental setup for ski-jump control of color centers in a diamond quantum microchiplet.

Fig. S4 shows the experimental setup used in the excitation of negatively charged silicon vacancy (SiV) color centers in a diamond quantum microchiplet (QMC) using a ski-jump device. Here, we used a wire-bonded, optically packaged device using a grating-coupled fiber which routes light to the ski-jump (950 µm long, 90 µm wide, 0.75 µm wide cross-ribs pitched at 4 µm, and a 300 nm thick and 400 nm wide Si_3N_4 waveguide with a taper to a 200 nm final width at the ski-jump's tip). There are two waveguides on this device, but we only use one for qubit control in this experiment.

Tunable laser light at ~737 nm from an M Squared SolsTiS module was routed to the ski-jump using the optically packaged grating-coupled fiber. A 50×, 0.55 NA, long working distance, infinity corrected objective was used to collect the ski-jump's optical output. The optical signal was then routed in free-space to the Montana cryostat containing the QMC. A similar 50× objective was used to focus the beam onto the waveguide channels. An OBIS 532 nm laser, gated by an AOM, was focused onto the entire QMC from a side window to reset the SiV emitters as needed.

The ski-jump device was driven with an AC signal of 3.17 kHz at 100 Vpp. In this experiment, we took advantage of a second harmonic resonance which caused the to oscillate at 6.34 kHz with high displacement. For the time-resolved avalanche photodiode (APD) measurements (Fig. 5c), the emitter was positioned at the top of the beam streak so that the emitter would be excited once per oscillation.

SiV sideband emission was routed to a fiber-coupled APD connected to an IDQ time-tagger for high resolution time-gated measurements. For $g^{(2)}(0)$ second order auto-correlation measurements, two fiber-coupled APDs were used with the optical signal separated by a 50:50 fiber splitter. SiV ensemble emission from individual waveguide channels was routed to an Andor ICCD (DH334T-18F-73, 1024x1024 pixels, 13x13 μm pixel size, 5 ns minimum gate width).

SI-8: Calculation of scan speeds and comparison to MEMS mirrors

For 2D MEMS mirrors and other pupil plane scanners, the scan range, pixel density, scan speed, refresh rates, and capacity can be calculated based on the following factors: angular scanning ranges (θ_{scanX} and θ_{scanY}), angular spot sizes (θ_{spotX} and θ_{spotY}), angular drive frequencies (ω_X and ω_Y, with $\omega = 2\pi f$), and device area. Using the following equations, we calculate the scan range as the number of resolvable beam spots from a single device, the pixel density as the number of beam spots that can be projected from 1 mm^2 chip footprint, the scan speed as the RMS of beam spots projected per second, the refresh rate in Hz, and the device capacity (our Figure of Merit) as the number of beam spots per second projected from a 1 mm^2 of chip area:

$$scan\_range\ [beam\ spots] = \frac{\theta_{scanX}}{\theta_{spotX}} * \frac{\theta_{scanY}}{\theta_{spotY}}$$

$$pixel\_density\ [beam\ spots/mm^2] = \frac{scan\_range}{device\_area}$$

$$scan\_speed\ [beam\ spots/sec] = \sqrt{\left[\frac{1}{\sqrt{2}}\frac{\theta_{scanX}}{2\theta_{spotX}}\omega_X\right]^2 + \left[\frac{1}{\sqrt{2}}\frac{\theta_{scanY}}{2\theta_{spotY}}\omega_Y\right]^2}$$

$$refresh\_rate\ [Hz] = scan\_speed/scan\_range$$

$$device\_capacity\ [beam\ spots/(sec * mm^2)] = scan\_speed * refresh\_rate$$

Similar metrics can be used to calculate the scan range based on the displacement of the waveguide tip for focal plane scanners, which we measure by measuring the beam trajectory on our ICCD (i.e. the beam's full range of motion on resonance). With this, we calculate scan range, pixel density, scan speed, refresh rates, and device capacity based on the following factors:

waveguide tip displacement (d_{scanX} and d_{scanY}), waveguide emitted spot size (d_{spotX} and d_{spotY}), angular drive frequencies (ω_X and ω_Y, with $\omega = 2\pi f$), and device area:

$$scan\_range\ [beam\ spots] = \frac{d_{scanX}}{d_{spotX}} * \frac{d_{scanY}}{d_{spotY}}$$

$$pixel\_density\ [beam\ spots/mm^2\ footprint] = \frac{scan\_range}{device\_area}$$

$$scan\_speed\ [beam\ spots/sec] = \sqrt{\left[\frac{1}{\sqrt{2}}\frac{d_{scanX}}{2d_{spotX}}\omega_X\right]^2 + \left[\frac{1}{\sqrt{2}}\frac{d_{scanY}}{2d_{spotY}}\omega_Y\right]^2}$$

$$refresh\_rate\ [Hz] = scan\_speed/scan\_range$$

$$device\_capacity\ [beam\ spots/(sec * mm^2)] = scan\_speed * refresh\_rate$$

For our device, we use $d_{spotX} = 0.56\ \mu m$, $d_{spotY} = 0.42\ \mu m$ (further discussed in SI-9). We collect 2D scan data from a split-electrode device at vacuum by measuring the 2D scan range on an ICCD (Fig. 4d) with various drive voltages. We use frequencies around the second longitudinal resonance (approx 6.6 kHz) and first lateral resonance (approx 4.9 kHz), but adjust the frequency to maximize the projected area. We then use the measured average X and Y displacement to calculate the scan range (in beam-spots), full-fill refresh rates (in Hz), RMS scan speed (in spots/second), and beam-spot capacity (in spots/(sec-mm^2)). These values are shown in Table S2.

Table S2: Calculated device scanning metrics
(*$d_{spotX} = 0.56\ \mu m$; $d_{spotY} = 0.42\ \mu m$; device size=0.1 mm^2*)

f_X (kHz)	$V_{pk\text{-}pk\ X}$ (V)	d_{scanX} (µm)	f_Y (kHz)	$V_{pk\text{-}pk\ Y}$ (V)	d_{scanY} (µm)	2D Scan Range (spots)	Pixel Density (spots/mm^2)	Scan Speed (rms spots/sec)	Refresh Rate (Hz)	Device Capacity (spots/sec-mm^2)
4.975	1	37	**6.658**	1	63	9,900	99,000	2.34E6	236	2.34E7
4.938	2	52	**6.615**	2	60	13,064	130,640	2.32E6	177	2.32E7
4.864	5	71	**6.514**	5	119	35,658	356,580	4.32E6	121	4.32E7
4.720	10	106	**6.333**	10	196	88,074	880,740	6.85E6	78	6.85E7
4.697	30	140	**6.296**	30	191	113,500	1,135,000	6.86E6	60	6.86E7

We note that the refresh rate and pixel density is for a scan that maximizes the number of spots at a given drive voltage and scan range. If a lower fill factor and higher refresh rate were desired, we could increase our refresh rate while lowering the number of spots, but the scan speed and device capacity would remain approximately the same. For these metrics, we note that increasing the drive frequencies, increasing the scan range, decreasing the device area, and increasing the number of waveguides per device are all potential ways to improve the refresh rate, pixel density, scan speeds, and device capacity.

The derivation for an analytical expression of the FoM can be obtained using expressions for the amplitude and frequency of a cantilever beam under forced sinusoidal drive on resonance given in chapter 11 of ref. [48].

$$FoM_{1D} = a_n \omega_n / (LWd_{spot}) = \left[\frac{fL^4 Q}{EI(n\pi)^4}\right] \times \left[(n\pi)^2 \sqrt{\frac{EI}{\rho A L^4}}\right] / (LWd_{spot}) = \frac{2Q_n \beta V}{(n\pi)^2 d_{spot}} \sqrt{\frac{3}{E\rho}} \left(\frac{L}{Wh^2}\right)$$

where a_n, ω_n, and Q_n are the amplitude, resonant frequency and quality factor of the n^{th} resonance, and d_{spot} is the waveguide mode spot size. L, W, h, E and ϱ are the length, width, thickness, effective Young's Modulus and density of the cantilever and $I = Wh^3/12$ is the area moment of inertia. $f = \sigma W$ is the force per unit length of the cantilever in the direction of motion. $\sigma = \beta V$ is the component of the induced stress parallel to the direction of motion. V is the applied voltage and the coefficient β is empirically calculated using static beam deflection analysis, $\delta = fL^4/(8EI)$, from the DC deflection data in Fig. 2g to be β = 1.76e-4 Pa/V. Fig. S5 plots the FoM_{1D} with the data from Fig. 3c for the n = 2 longitudinal mode in vacuum, i.e. no free or fitted parameters. We see good agreement for low voltages; however, we observe deviation at higher voltages which we attribute to mechanical nonlinearities and a greater difficulty in achieving and maintaining peak resonant driving of high-Q resonances (due to the onset of both thermal and mechanical nonlinearities).

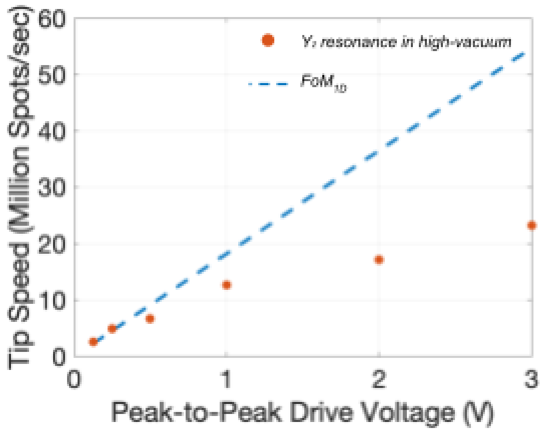

Fig. S5 | Tip speed as calculated using characterization of the Y_2 mechanical resonance in high-vacuum conditions, as shown in Fig. 3c.

SI-9: Optical mode of the ski-jump

Throughout this paper, all devices use Si_3N_4 as the waveguide core with SiO_2 cladding on all sides. The waveguide core of these devices is 400 nm wide and 300 nm thick with an optional adiabatic taper to a 200 nm width at the tip. This taper was included on all devices discussed except for the broadband demonstration shown in Fig. 3g. (This was coincidental; the broadband demonstration could have been done with a tapered waveguide.) These waveguide dimensions and materials are not fundamental to this beam scanning technology, allowing for flexibility in the optical mode design for any given application. The simulated mode of the untapered waveguide, shown in Fig. S6a, has a horizontal beam waist w_x=0.28 µm and a vertical beam waist w_y=0.21 µm with divergence half-angles of θ_x=48° and θ_y=65°. For the simulated mode of the tapered waveguide, shown in Fig. S6b, w_x=0.33 µm, w_y=0.25 µm, θ_x=41°, and θ_y=53°.

For the experimental imaged beam-spot measurements noted in the following discussion, the ski-jump waveguide was tapered. For characterization of the ski-jump's optical output with λ=737 nm: we used a 100✕, 0.9 NA objective (Nikon U Plan Fluor Infinity-Corrected) to collect and collimate the light before refocusing it onto a CMOS camera (Thorlabs CS165MU). The objective was mounted on a piezoelectric positioning collar which enabled adjustments to the distance between the objective and ski-jump tip with a precision of 1 nm/mV. The ski-jump's optical output was imaged at various objective heights, covering more than the Rayleigh range, and the data was then fit to Gaussian beam propagation equations. We experimentally measure beam waists of w_x=0.40 µm and w_y=0.43 µm, respectively, as shown in Fig. S6c-d. The corresponding Rayleigh ranges are $z_{R,x}$=0.78 µm and $z_{R,y}$=0.94 µm with divergence half-angles of θ_x=60° and θ_y=53°. The slight ellipticity of the optical mode is due to the rectangular shape of the waveguide. We attribute the small offset of the beam waist position in the gaussian fit to imperfections in the imaging system, such as a residual relative tilting between the ski jump output direction and the optical axis. David Brinkmeier's laser beam analyzer (https://github.com/david-brinkmeier/fokuspokus) was used for analysis of the experimental optical mode data.

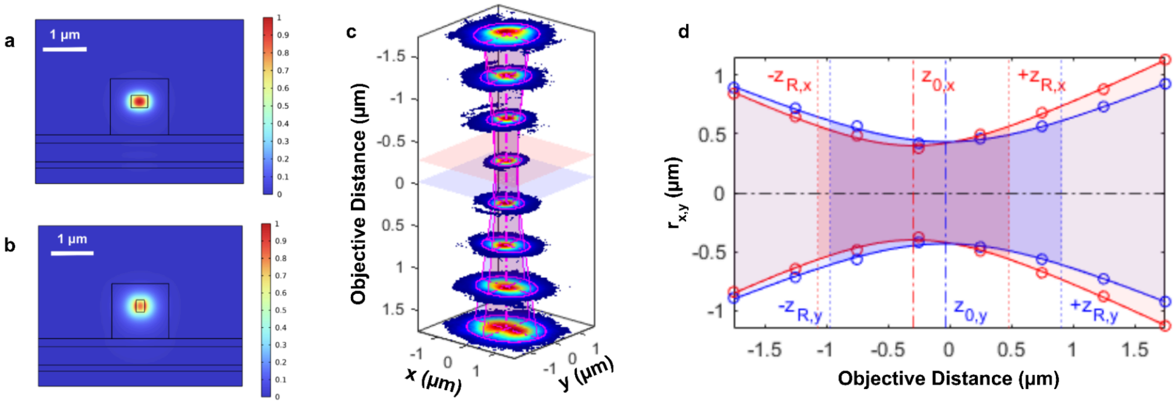

Fig. S6 | Optical output of the ski-jump waveguide. a, FEM simulation of the normalized electric field amplitude for the TE mode of a Si_3N_4 waveguide cladded in SiO_2 operating at 737 nm. The waveguide is 400 nm wide and 300 nm thick or **b,** 200 nm wide and 300 nm thick. **c,** Images of the imaged ski-jump optical mode as a function of distance between the ski-jump tip and the objective. **d,** Comparison of the horizontal (x) and vertical (y) mode profiles of the ski-jump as a function of distance between the ski-jump tip and the objective.

SI-10: Post-fabrication tuning of the cantilever’s passive curvature

Though we did not need to post-process any of the ski-jumps discussed in this manuscript, it is useful to have simple methods available for post-fabrication adjustment to the ski-jump’s passive curvature. One method for adjusting the cantilever’s passive curvature post-fabrication is to alter the SiO_2 cross-rib patterning. Though this could be done in a number of ways, we demonstrated this using reactive ion etching (RIE) to globally reduce the SiO_2 thickness on the devices. In these examples, shown in Fig. S7, the thinning out of the SiO_2 cross-ribs reduced the radius of curvature for the devices, indicating that the initial thickness of the cross-ribs was not perfectly optimized to enhance longitudinal curvature. Similarly, localized etching of the cross-rib patterning could be done device-to-device in cases where a global adjustment to the entire PIC is not desired.

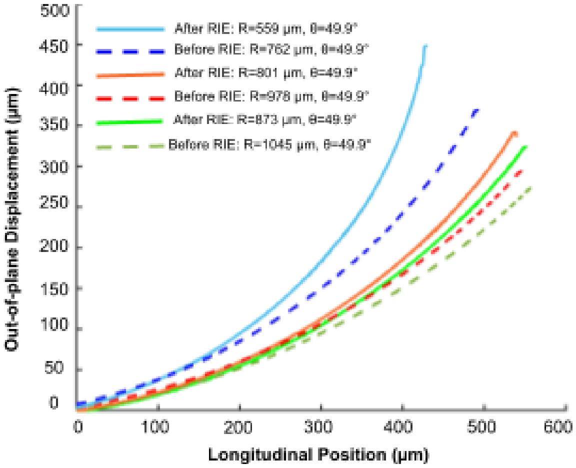

Fig. S7 | Post-fabrication tuning of passive cantilever curvature with RIE. Longitudinal surface profile along the cantilever’s midline. This measurement was done using a white light profilometer. These devices are 800 µm long with 1 µm wide crossbars and a 2 µm period. Cantilever widths are 50 µm (green), 70 µm (red/orange), and 90 µm (blue).

SI-11: Optical Loss Characterization

The current devices were fabricated with a narrow waveguide cladding width of 1.4 µm. However, the release process weakly etches silica and therefore reduced this width further down to 1.2 µm, resulting in an overexposed optical mode. As a result, we observe scattering loss at the waveguide-cross rib anchor points where there is both a large index and strain gradient, leading to widely-varying transmission loss between devices. We can observe this periodic scattering when looking at our device with an overhead camera.

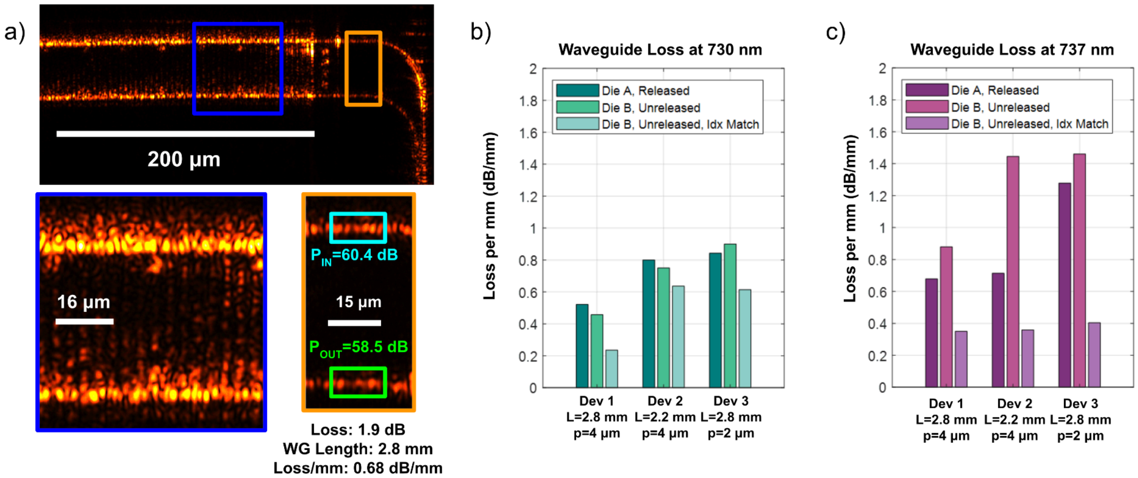

Fig. S8 | Ski-jump loss characterization. a, Overhead microscope view of a released device with 4 µm crossbar period, with zoom-in on device, showing high scattering in crossbars, and a power intensity measurement, taken as the sum of red pixels in the area, at waveguide input/output. **b-c,** Measured losses in dB/mm on 3 devices with 730 nm (b) and 737 nm light (c). Devices from released and unreleased dies show 0.5-1.4 dB/mm of loss. Adding an index matching coating over the devices reduced loss to ~0.5 dB/mm.

We show the high scattering in crossbars and our methodology for measuring device loss in Fig. S8a. In order to determine the loss in our device, we perform loss characterization on a set of devices with a looping waveguide in the cantilever. To estimate the loss, we use an overhead camera (Pixelink DL-7620 with no IR Cutoff filter) to observe scattering in the input and output waveguide. We measure the sum of the red pixel intensity and calculate the loss in dB, and divide that by the waveguide length in our device to measure loss in dB/mm. To reduce the scattering from the change in index at crossbars, we apply a gel serving as an index-matching coating (Dymax OP-29) over the unreleased ski-jump devices and measure a noticeable decrease in device loss.

Fig. S8b shows measured loss at 730 nm laser light. Released and unreleased devices show 0.5 to 0.9 dB/mm of loss, while applying an index-matching coating to an unreleased device decreases loss to 0.2-0.6 dB/mm. Fig. S8c shows measured loss at 737 nm laser light. Here, released and unreleased devices show 0.6-1.4 dB/mm of loss, and applying an index-matching coating decreases loss to 0.3-0.4 dB/mm. With the index matching coating, our device's optical loss is comparable to loss measured in the silicon nitride waveguides on our PIC platform.